

# A study of matching fluid loss in a biomedical microwave tomography system

Colin Gilmore<sup>a)</sup>

TRLabs, Winnipeg, Manitoba, Canada, R3T 6A8

Amer Zakaria and Joe LoVetri

Department of Electrical and Computer Engineering, University of Manitoba, Manitoba, Canada, R3T 5V6

Stephen Pistorius

CancerCare Manitoba and the Department of Physics and Astronomy, University of Manitoba, Manitoba, Canada, R3T 2N2

(Received 4 July 2012; revised 14 December 2012; accepted for publication 14 December 2012; published 25 January 2013)

**Purpose:** Effective imaging of human tissue with microwave tomography systems requires a matching fluid to reduce the wave reflections at the tissue boundary. Further, in order to match the idealized mathematical model used for imaging with the complicated physical measurement environment, loss must be added to the matching fluid. Both too little and too much loss result in low-quality images, but due to the nonlinear nature of the imaging problem, the exact nature of loss-to-image quality cannot be predicted *a priori*. Possible optimal loss levels include a single, highly sensitive value, or a broad range of acceptable losses. Herein, the authors outline a process of determining an appropriate level of loss inside the matching fluid and attempt to determine the bounds for which the images are the highest quality.

**Methods:** Our biomedical microwave tomography system is designed for 2D limb imaging, operating from 0.8 to 1.2 GHz. Our matching fluid consists of deionized water with various levels of loss introduced by the addition of table salt. Using two homogeneous tissue-mimicking phantoms, and eight different matching fluids of varying salt concentrations, the authors introduce quantitative image quality metrics based on  $L$ -norms, mean values, and standard deviations to test the tomography system and assess image quality. Images are generated with a balanced multiplicative regularized contrast source inversion algorithm. The authors further generate images of a human forearm which may be analyzed qualitatively.

**Results:** The image metrics for the phantoms support the claim that the worst images occur at the extremes of high and low salt concentrations. Importantly, the image metrics show that there exists a broad range of salt concentrations that result in high-quality images, not a single optimal value. In particular, 2.5–4.5 g of table salt per liter of deionized water provide the best reconstruction quality for simple phantoms. The authors argue that qualitatively, the human forearm data provide the best images at approximately the same salt concentrations.

**Conclusions:** There exists a relatively large-range of matching fluid losses (i.e., salt concentrations) that provide similar image quality. In particular, it is not necessary to spend time highly optimizing the level of loss in the matching fluid. © 2013 American Association of Physicists in Medicine. [<http://dx.doi.org/10.1118/1.4788640>]

Key words: microwave imaging, electromagnetic tomography

## I. INTRODUCTION

Microwave tomography (MWT) shows promise as an alternative biomedical imaging modality. Clinical applications of MWT (and in imaging with microwaves in general) include assessment of soft-tissue injuries<sup>1,2</sup> and extensive research into breast cancer (for examples, see Refs. 3–5, 8, and 10–15). MWT is nonionizing, low cost, exploits a contrast mechanism unique to the modality, is capable of soft tissue contrast, and can create quantitative (as opposed to qualitative) images. Despite these advantages, MWT has not seen widespread clinical use (e.g., it is not regularly used in hospitals or other clinics), and is still under active investigation.

In this paper, we study the effects of loss in the matching fluid used in an experimental MWT system designed for limb imaging. Systems such as these (a) provide the ability to image human patients, generating interest from clinical professionals, (b) provide new experimental data, leading to new applications for microwave imaging, and (c) provide the experimental data necessary to test and drive innovation in inversion algorithms.

For effective biomedical microwave imaging, a matching fluid is used to reduce the contrast between human tissue and the background where the imaging experiment occurs (see, e.g., Refs. 6, and 16–18). Current tomographic imaging algorithms cannot effectively image the interior of a biological

target in an air background, even when low-noise synthetic data are used. The matching fluid may be viewed as both increasing the amount of detectable energy interacting with (and inside) the target, and/or reducing the contrast in the mathematical reconstruction problem.

For our system, we use a matching fluid of water, which is readily available, easily disposable, and a reasonable permittivity to match to many human tissues. Where some tissues (i.e., adipose) have a high contrast with water, the water may be mixed with glycerol or other water-soluble liquid which reduces the contrast with respect to those tissues.<sup>1,2,16</sup> Other studies have considered various commercially available lotions and sunscreens<sup>7</sup> or simulated oils.<sup>6</sup> However, none of these studies have considered optimizing the loss of the matching fluid to improve the image quality. Overall, previous studies are mostly concerned with reducing the tissue-background contrast. We also note that one alternative to matching fluids is the use of contact-based antennas (e.g., Refs. 9, 14, and 15), but to-date these types of systems are based on linear imaging techniques that do not provide quantitative images and are left as out-of-scope for this work.

Further to the use of a matching fluid to reduce the image contrast, it is also desirable to add loss to the fluid. A simple way of accomplishing this in water is to add table salt (sodium chloride) to the fluid, which has the effect of both increasing the operating bandwidth of the antennas,<sup>19</sup> and reducing the *modeling error*: errors caused by a mismatch between the assumed electromagnetic model in the inversion algorithm and the actual physical system. Examples of modeling errors include the reflections from nonactive antennas, reflections from the bottom and top of the imaging chamber, incident field assumption errors, the use 2D imaging algorithms, and reflections from the chamber wall.<sup>16,20</sup> While some of these errors can be eliminated through better modeling (e.g., including the chamber wall<sup>21–24</sup> or modeling antennas,<sup>25–27</sup> or using a 3D inverse solver<sup>28–31</sup> and modeling the whole system in the inversion), in general these errors can be reduced by simply adding loss to the matching fluid, which has the advantage of simplicity and not requiring additional computation resources. However, the addition of loss involves a trade-off: the salt also reduces the level of the desired signal which is necessary to image the target. If enough salt is added, the received signal will be dominated by noise. Thus, the amount of salt added to the matching fluid must be optimized.

While poor image quality may seem to be an obvious result for the extremes of low and high loss matching fluids (particularly for high loss), there are many possibilities for the midrange of fluid loss. Two different possibilities for image error vs matching fluid loss are shown in Fig. 1 (in this figure, an example of “image error” could be an  $L$ -norm). One possibility is that there is a single narrow optimum for the matching fluid loss, which must be used for the best image quality. Another possibility is that there is a broad range of losses which result in a similar image quality. The form of the curve has significant repercussions for practical MWT: in the first case, (i) the MWT user needs to carefully select, control, and maintain (via regular measurement) the exact matching fluid loss. In the second case, (ii) a user may just add salt un-

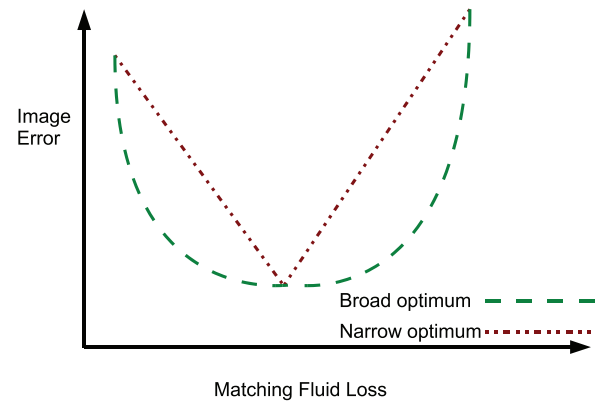


FIG. 1. Two different possibilities of the curve relating to image error vs matching fluid loss. A broad optimum allows for a range of reasonable matching fluid losses.

til the loss is somewhere within a broad range, then image a patient. Further, there is no way to know *a priori* the exact relationship between imaging quality and matching fluid loss for a given MWT system, without actually doing an experimental study. It is possible to perform analytic studies when attempting to find the maximum coupling of energy between the matching fluid and some specified tissue (e.g., Ref. 32), but the experimental imaging involves complex interactions between coupling energy, imaging algorithm, and modeling error, which is best studied empirically.

In this paper, we explore the trade-offs associated with the addition of loss to the matching fluid for MWT, and attempt to fill in the image quality curve shown in Fig. 1. The first contribution of this work is the definition of empirical metrics by which we can quantify image quality. This is accomplished by using two muscle tissue mimicking phantoms, and defining quantitative metrics of reconstruction quality and noise in the received signal. The phantoms are imaged for a series of salt concentrations in the matching fluid, and the image metrics are used to show the second contribution: that there exists a wide-range of salt concentrations which provide similar high-quality images. Simple phantoms are selected for this process, because of the difficulty in defining and applying quantitative metrics to more complicated phantoms. To provide results for a more complicated, realistic scenario, the quantitative results are supplemented by a qualitative analysis of human forearm data collected with the same imaging system at the same salt concentrations.

The paper is organized as follows. In Secs. II–IV we define our assumptions, give a brief description of the imaging algorithm, describe the matching fluids used for the study, and provide an overview of the tomography system. In Sec. V we discuss the phantoms and define our image metrics used to quantitatively assess image quality. In Sec. VI we describe our results which are discussed in Sec. VII. Finally, the paper is concluded in Sec. VIII.

## II. INVERSE PROBLEM AND PERMITTIVITY DEFINITIONS

For our reconstructions, we assume a 2D scalar problem (transverse magnetic polarization), and an  $\exp(j\omega t)$  time

dependence. The governing equation is the integral form of the 2D scalar Helmholtz equation:

$$u^{\text{sct}}(\mathbf{r}) = \int_D G(\mathbf{r}, \mathbf{r}') \chi(\mathbf{r}') u^{\text{tot}}(\mathbf{r}') d\mathbf{r}' \quad \mathbf{r} \in S, D, \quad (1)$$

where  $u^{\text{sct}}$  and  $u^{\text{tot}}$  are the scattered and total fields,  $G(\mathbf{r}, \mathbf{r}')$  is the Green's function,  $D$  represents the imaging domain, and  $S$  represents the measurement domain. The contrast is given by

$$\chi(\mathbf{r}) = (\epsilon(\mathbf{r}) - \epsilon_b) / \epsilon_b, \quad (2)$$

where  $\epsilon(\mathbf{r})$  and  $\epsilon_b$  are the complex permittivity of the target and background, respectively. We model complex permittivity by

$$\epsilon(\mathbf{r}) = \epsilon_0(\epsilon' - j\epsilon'') = \epsilon_0 \left( \epsilon' - j \frac{\sigma_{\text{eff}}}{\omega \epsilon_0} \right), \quad (3)$$

where  $\omega$  is the angular frequency and  $\sigma_{\text{eff}}$  is the effective conductivity. In general, both  $\epsilon'$  and  $\sigma_{\text{eff}}$  vary with frequency. While not strictly correct, for simplicity we use the word “permittivity” to refer to the relative permittivity for the remainder of this document.

### II.A. Inversion algorithm

All inversions in this work were performed with the balanced multiplicatively regularized contrast source inversion (BMR-CSI) technique.<sup>33</sup> The algorithm is based on the multiplicatively regularized contrast source inversion technique.<sup>34,35</sup> However, similar to some other algorithms,<sup>36,37</sup> the real and imaginary parts of the contrast are scaled with a balancing factor, which ensures that the multiplicative regularizer used in the cost functional provides a more balanced weight to the real and imaginary parts of the permittivity. Balanced algorithms such as these are useful when the real and imaginary parts of the permittivity have a large difference in magnitude. As per the empirical methods discussed in Ref. 33, we select the balancing factor to be equal to the ratio of the real to imaginary part of the permittivity of

TABLE I. Matching fluid labels and details. Fluids were chosen, and are labeled, based on the approximate value of  $\epsilon''$  of the solution at 1 GHz. See Eq. (3) for definition of  $\epsilon''$ .

Data set label	Total amount of salt (g) $\pm 0.5$ (g)	Salt per liter (g/l)
<i>Salt 4</i>	0	0
<i>Salt 10</i>	120	1.71
<i>Salt 12.5</i>	175	2.5
<i>Salt 15</i>	220	3.14
<i>Salt 17.5</i>	277	3.96
<i>Salt 20</i>	330	4.72
<i>Salt 22.5</i>	380	5.43
<i>Salt 25</i>	450	6.43

our target phantom. When used in biomedical imaging, this balancing factor may be set to the approximate ratio for the tissues being imaged.

### III. DESCRIPTION OF MATCHING FLUIDS

Table I lists the eight different matching fluids which are used throughout this work. The fluids were selected, and are labeled, based on the approximate value of the imaginary part of the permittivity at 1 GHz. The solutions were created by adding table salt to deionized water as per Table I. Table salt contains anticaking agents and is not pure NaCl. However, as we are aiming at particular permittivities (not an exact concentration of salt), the main desired result (the addition of loss to the fluid) is obtained.

A plot of the permittivities over the frequency range from 600 MHz to 1.6 GHz is shown in Fig. 2. These frequencies were selected as the approximate bandwidth of the antennas inside our imaging system. All measurements were made with an Agilent 85070 open-ended coaxial performance probe. The addition of salt has a small effect on the real part of the permittivity, and a large effect on the imaginary part of the permittivity (loss). Figure 3 shows the imaginary part of the

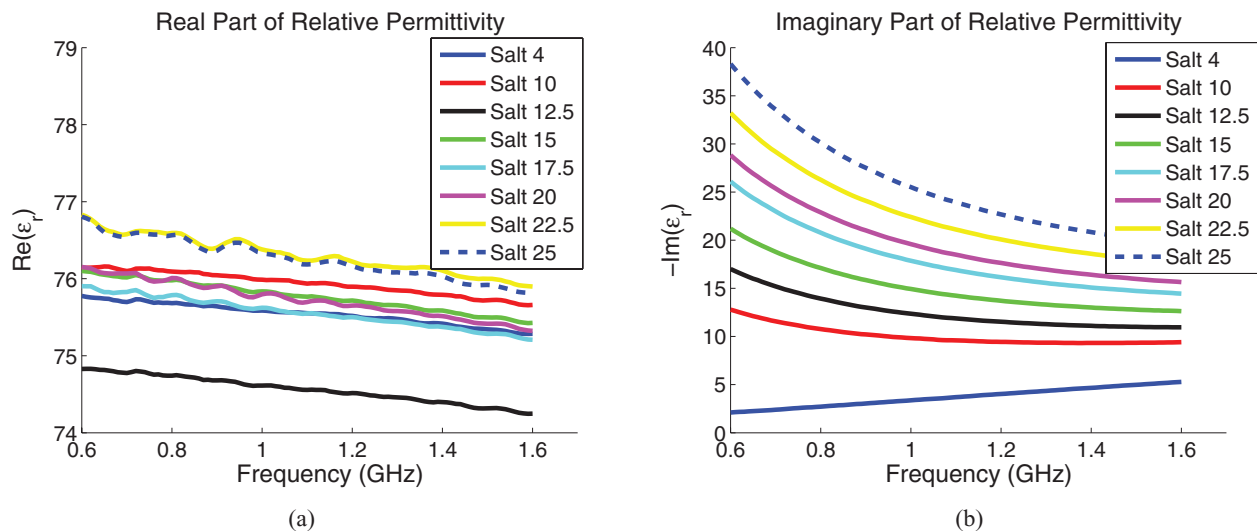


FIG. 2. Complex permittivity of the various matching fluids. (a) The real part of the permittivity and (b) the imaginary part of the permittivity.

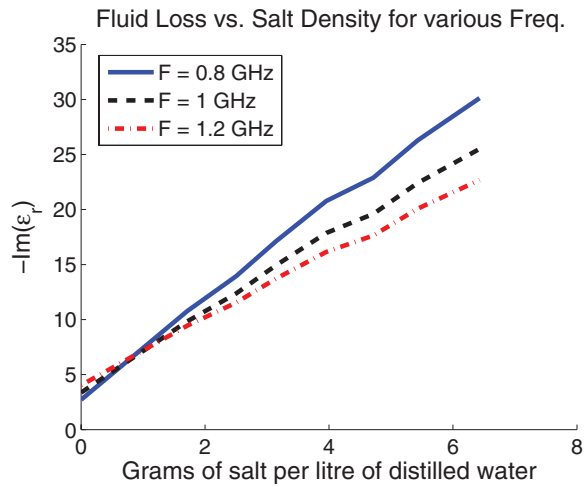


FIG. 3. Imaginary part of permittivity vs table salt density for 0.8, 1, and 1.2 GHz.



FIG. 4. Photograph of apparatus with a glycerol/water-based phantom.



(a)



(b)

FIG. 5. (a) Photograph of a single antenna element and (b) the two imaging phantoms. Phantom 1 is shown on the left, and phantom 2 is shown on the right. The bottles are the same, with different fluids inside.

permittivity vs table salt density, for frequencies of 0.8, 1, and 1.2 GHz.

#### IV. OVERVIEW OF SYSTEM

The experimental system consists of an Agilent PNA network analyzer (E8363) (the microwave source and receiver) connected to 24 antennas via a  $2 \times 24$  matrix switch (Agilent 87050A-K24), which provides isolation of greater than 95 dB over the frequency range of interest. Twenty-four antennas are arranged at even intervals of  $15^\circ$  in a circular array at the mid-point height along the inside of a metallic cylinder. Each antenna is connected with a cable (Pasternack Enterprises PE-300-60), with greater than 100 dB shielding. The antennas are located at a radius of 9.4 cm from the center of the chamber. The enclosure has a radius of 22.4 cm and is filled, to a height of 44.4 cm, with the matching fluid. Figure 4 shows a photograph of MWT system with a tissue-mimicking glycerol/water based imaging phantom in the imaging region. The total volume of fluid in the chamber is approximately 70.0 l.

The experimental apparatus is controlled via a computer workstation which is connected through a local-ethernet device. In-house developed software is used to collect the data set for each desired image. Data acquisition for 20 discrete frequencies takes less than 1 min to acquire ( $24 \times 23$  measurements per frequency).

##### IV.A. Antenna design

Our antennas consist of dipoles with a matching balun. The dipole's arms and the balun are 1.1 cm long, with a central operating frequency of approximately 1 GHz. A photograph of one of the antennas is shown in Fig. 5(a). The antennas are linearly polarized, oriented in the vertical ( $z$ ) direction, and extend approximately 13 cm into the enclosure (and are thus located on a circle of radius 9.4 cm). For each matching

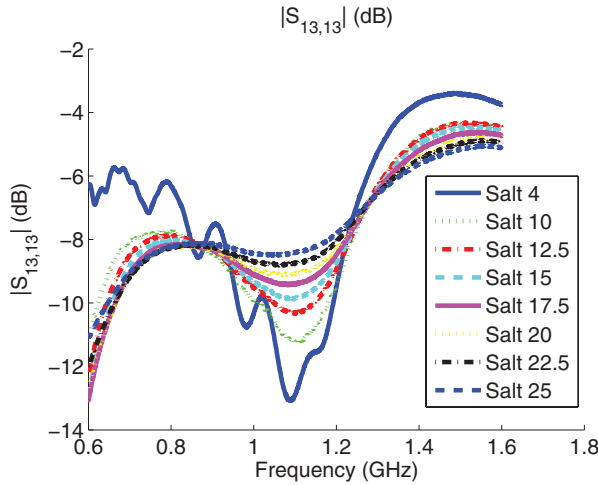


FIG. 6. A plot of  $|S_{13,13}|$  in dB for all matching fluids.

fluid, a plot of the magnitude of the return-loss ( $|S_{13,13}|$ ) is shown in Fig. 6. For *Salt 4*,  $|S_{13,13}|$  is below  $-10$  dB from approximately 0.9 to 1.15 GHz. The addition of salt to the matching fluid improves the ability of the antenna to radiate into the fluid at higher and lower frequencies, while lowering the amount of energy radiated at the center frequency. We note that the antenna bandwidth does not necessarily correlate with good imaging frequencies, see, e.g., Ref. 38. There are many other factors which can affect the imaging result, and well matched antenna is only a necessary condition.

#### IV.B. Modeling error, system model, and simulation

In order to show that modeling error is present at low salt concentration, we investigate the normalized measured  $S$ -parameters and assumed incident field in the imaging algorithm on the measurement surface  $S$ . Furthermore, in order to confirm that our experimental system is working as expected, we also consider a FEKO-based computational model of the MWT system. The model consists of the metallic chamber, filled with the matching fluid, with 24 wire dipoles (with feed points in the middle of the wire). The FEKO model does not contain any of the backing wires to the individual antennas. There was no imaging target present in the simulation. The system was simulated at a frequency of 1 GHz.

A comparison of  $|S_{1,x}|$  for a few selected fluids is shown in Fig. 7. The values of  $|S_{1,x}|$  for the analytic line source model used in the inversion algorithm is also shown in Fig. 7. In our experience, the closer the measurement to the incident field, the better the inversion result (all else being equal). For each subfigure, the data sets were normalized to the measurement data. Figure 7 illustrates the modeling error: when using deionized water ( $\epsilon = 77.7 - j3.8$ ) there are still resonant modes which increase the difference between the analytic field and the measurements ( $L_2$  norm of 0.66%). The *Salt 15* ( $\epsilon = 77.0 - j14.6$ ) measurement more closely matches the analytic solution ( $L_2$  norm of 0.16%), and the *Salt 20* ( $\epsilon = 76.9 - j20.7$ ) measurement is similar to *Salt 15* ( $L_2$  norm 0.15%). While both the lossy data sets match the

analytic solution, the *Salt 20* data set has an  $S_{1,13}$  of nearly  $-90$  dB, which is approaching the dynamic range of the switch ( $\sim 95$  dB over the frequency range of interest). We also note that scattered fields can be expected to have a lower magnitude than the incident fields.

## V. PHANTOMS AND QUALITY METRICS

The two phantoms which were used for testing are shown in Fig. 5. Each phantom was filled with a glycerol/deionized water solution of differing concentrations. The permittivity profiles of the two phantoms are shown in Figs. 8(a) and 8(b). The exact proportions of glycerol and water were not measured. The phantoms have a measured diameter of 73.5 mm, and when in the imaging system, the  $z$ -plane of the antennas was located 6.5 cm from the bottom of the bottle (just above the text “University of Manitoba”).

The advantage of simple phantoms is that “ideal” images may be defined. For these phantoms, we define the ideal reconstruction as a circle of radius equal to the outside radius of each phantom (at the same elevation as the antennas), with a permittivity equal to the measured permittivity shown in Fig. 8. The thin plastic bottle wall ( $\approx 1$  mm) is ignored in the ideal reconstruction, as it is less than  $1/25$  of the minimum wavelength. An example of an “ideal” image is shown in Fig. 9.

In order to appropriately apply the image quality metrics, the ideal location of the phantom needs to be placed into the image. The center of the ideal phantom image was manually collocated on the physical position of the phantom via a simultaneous viewing of highly enlarged images of the experimental reconstruction and ideal image. Automatic methods (e.g., using an autocorrelation of the two images and selecting the peak value as the best match) were attempted, but were not as accurate as the manual procedure. We recognize that this could induce bias to our results, but the alternative of measuring the physical position of the phantom (a) could also be biased and (b) is impractical in the matching fluid given the multiple measurements needed for calibration and determining scattered fields.

#### V.A. Image metrics

Each reconstruction image was split into two homogeneous regions: target and background, with the edges of the regions defined by the ideal image. For each region we compute the mean value and the standard deviation as well as the  $L_1$  and the  $L_2$  norm. As two distinct images (the real and imaginary parts of the permittivity) are reconstructed, we have found it useful to compute the  $L$ -norms of the real and imaginary parts separately. The  $L_n$  norm of the real part of the reconstruction  $Re(\epsilon_{\text{recon}})$  is defined as

$$L_n^{Re}(\epsilon_{\text{recon}}) = \left( \int |Re(\epsilon_{\text{recon}}(\mathbf{r})) - Re(\epsilon_{\text{ideal}}(\mathbf{r}))|^n d\mathbf{r} \right)^{1/n}, \quad (4)$$

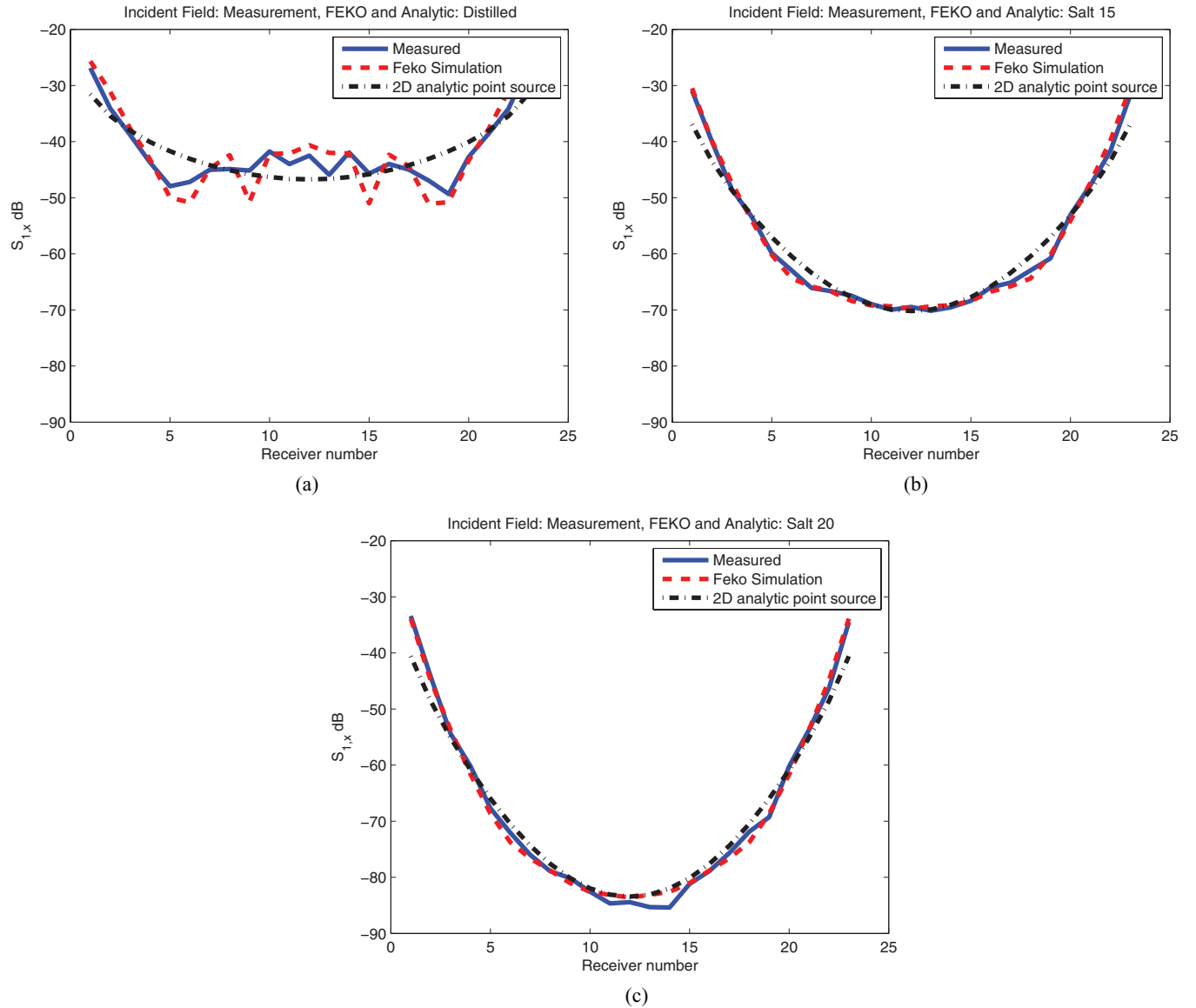


FIG. 7. Measurement vs simulation for the imaging system. (a) Deionized water, (b) *Salt 15* fluid, and (c) *Salt 20* fluid. Measurements are shown with a solid line, simulation results in a dashed line, and the 2D analytic point source in the dash-dot line. For each subfigure, the data sets were normalized to the measurement.

where  $\epsilon_{\text{recon}}$  and  $\epsilon_{\text{ideal}}$  are the reconstructed and ideal permittivities, respectively. Imaginary image metrics are similarly defined.

## V.B. Noise metric

To provide an estimate of the signal-to-noise ratio of the collected data, we define a noise metric,  $N$  as

$$N = \frac{1}{N_{x,y}} \sum_{x,y \text{ pairs}} \frac{\|S_{x,y}^{\text{sct}} - S_{y,x}^{\text{sct}}\|}{\|S_{x,y}^{\text{sct}}\|}, \quad (5)$$

where  $S_{x,y}^{\text{sct}}$  is the calibrated scattered field  $S$  measurement,  $N_{x,y}$  is the sum of all active transmitter and receive pairs  $(x, y)$ , and the sum is taken over all active pairs of  $x$  and  $y$ . We justify this metric since from reciprocity,  $S_{x,y} = S_{y,x}$ , and any-

thing else in the data must be noise. Further, this metric is very similar to the “data error term” in the inversion algorithm<sup>34,35</sup> including the fact that it does not differentiate between high- and low-power signals in the summation. This metric provides an estimate of the nonmodeling noise level of the data. Modeling error will not be accounted for in this noise. This metric is a measure of a number of things, including thermal noise, coupling errors, and external noise sources.

## VI. RESULTS

With each phantom placed in the imaging system, data were collected for all eight matching fluids and for frequencies from 0.8 to 1.2 GHz in 100 MHz steps. The BMR-CSI algorithm was run on each data set (independently for each frequency), with the permittivity constrained to the ranges

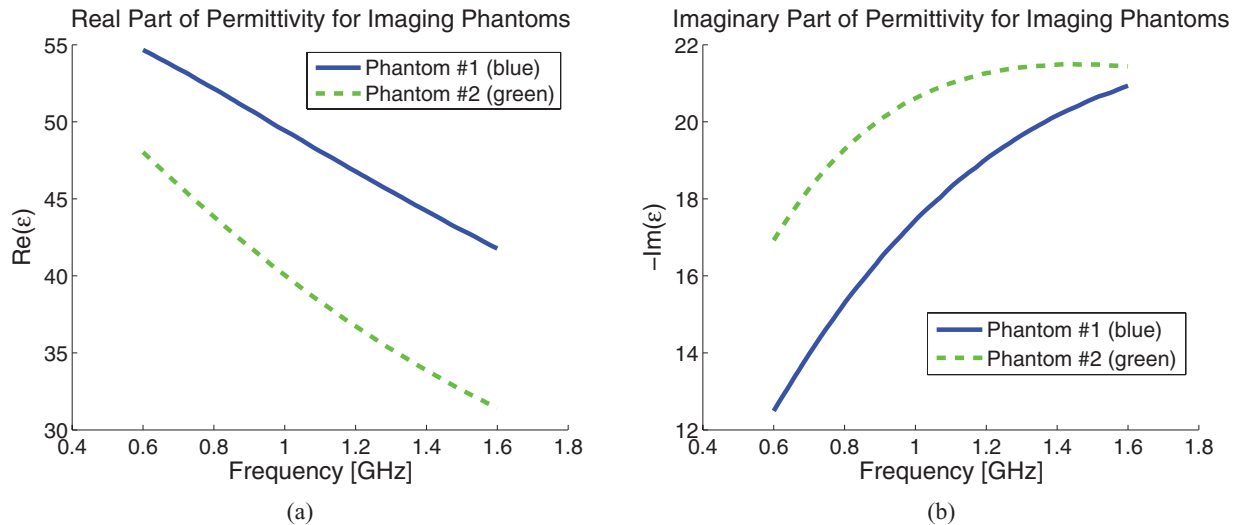


FIG. 8. Complex permittivity of the phantoms. (a) real and (b) imaginary.

$1 \leq Re(\epsilon) \leq 80$  and  $-30 \leq Im(\epsilon) \leq 0$ . The imaging region  $D$  was taken as a square with sides of length 12 cm. This results in 40 reconstructions, each with a real and imaginary part, and two reconstruction regions (target and background). We present imaging results for two cases: phantom #1 at 1 GHz and phantom #2 at 1.1 GHz. The image metrics are presented for all reconstructions.

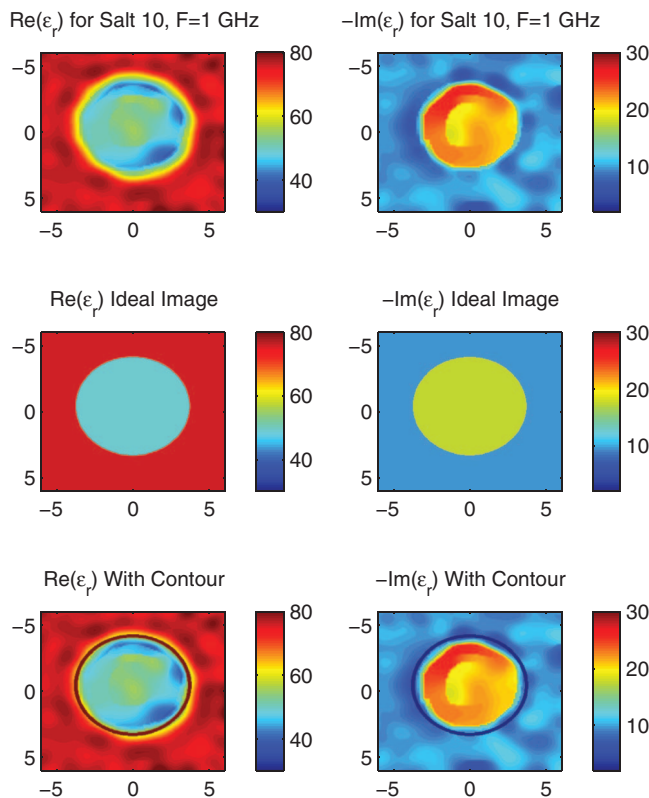


FIG. 9. Reconstruction of phantom #1, *Salt 10* data set at 1.0 GHz. The real and imaginary parts of the reconstruction are shown in the top row, the ideal image in the middle row, and an image with the contour from the ideal image superimposed in the third row. Axes are in cm.

### VI.A. Phantom #1

For the *Salt 10* matching fluid at 1 GHz, an image of the reconstruction, ideal image, and contoured image (where the ideal target contour is superimposed over the reconstruction), are shown in Fig. 9. The masked image is presented to help visualize the ideal image centering process.

The reconstructions of phantom #1 at 1 GHz for all eight matching fluids are shown in Figs. 10 and 11. Figure 12 shows the mean and standard deviations of the 1 GHz reconstructions (blue lines) and the measured permittivities (red “x”s) for both target and background (matching) fluids. For all data sets and frequencies, the  $L$ -norms are shown in Fig. 13. The errors between the measured permittivity and the average permittivity in each reconstruction region are plotted in Fig. 14. The noise metric for this data set is shown in Fig. 20(a).

### VI.B. Phantom #2

We also show the detailed results for phantom #2 at a frequency of 1.1 GHz. The image reconstructions are shown in Figs. 15 and 16, and the mean values with standard deviations (again for 1.1 GHz) are shown in Fig. 17. For all frequencies, the  $L$ -norms are shown in Fig. 18, the error between average region permittivity and the measured values are shown in Fig. 19, and the noise metric is shown in Fig. 20(b).

### VI.C. Human forearm results

The experiment process used for the phantoms was also repeated for a human forearm. This research was carried out under a University of Manitoba Biomedical Research Ethics Board approved protocol. The volunteer was a 32-year-old male, and we imaged his right arm. For space considerations, we present the full results for the arm data only at 1 GHz. For the balancing factor in the inversion algorithm, we selected  $Q = 5$ . Results for all eight matching fluids are shown in

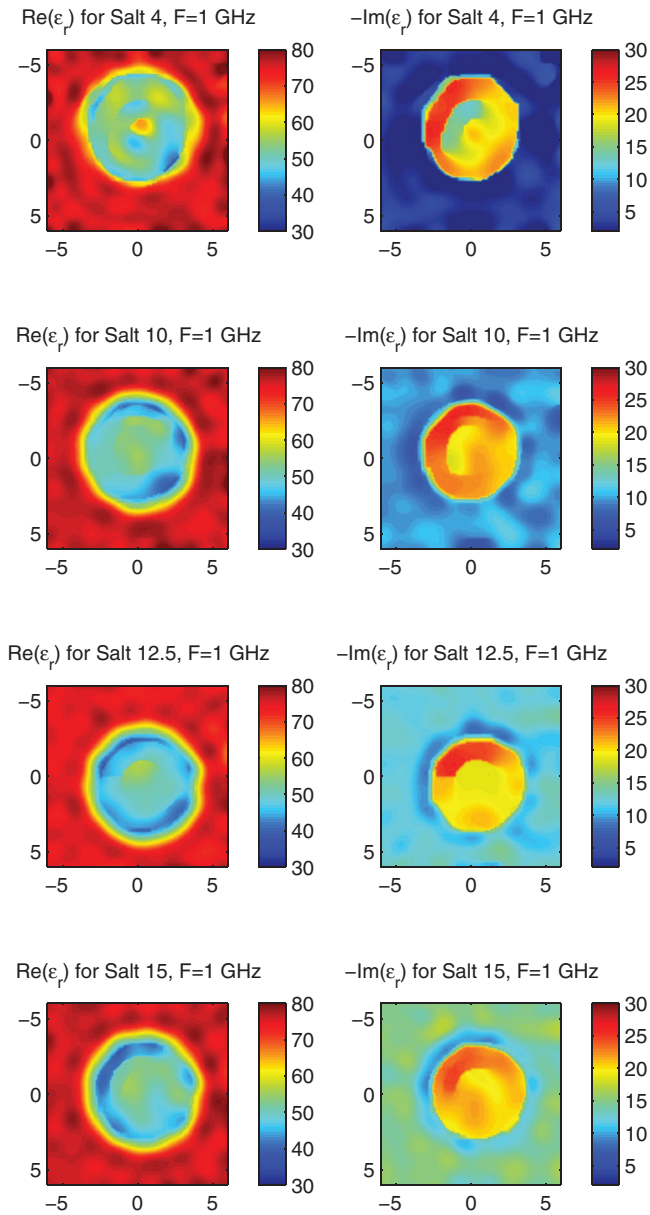


FIG. 10. Reconstruction of phantom #1 at 1.0 GHz, for four matching fluids, *Salt 4* through *Salt 15*. Real part of  $\epsilon$  is on the left and imaginary part on the right.

Figs. 21 and 22. The noise metric for all frequencies and salt concentrations is shown in Fig. 23.

## VII. DISCUSSION

Qualitatively, the trade-off between modeling error and loss is readily visible in the images for phantom #1 at 1 GHz and phantom #2 at 1.1 GHz, particularly for the imaginary part of the reconstruction (see Figs. 10, 11, 15, and 16). The low-loss *Salt 4* (deionized water) and the high-loss *Salt 25* data sets provide the worst reconstructions, the former due to high modeling error, and the latter due to high noise.

In general, the modeling-error/noise trade-off is also visible in the  $L$ -norm plots for all the frequencies, again particularly for the imaginary reconstructions (see Figs. 13 and 18).

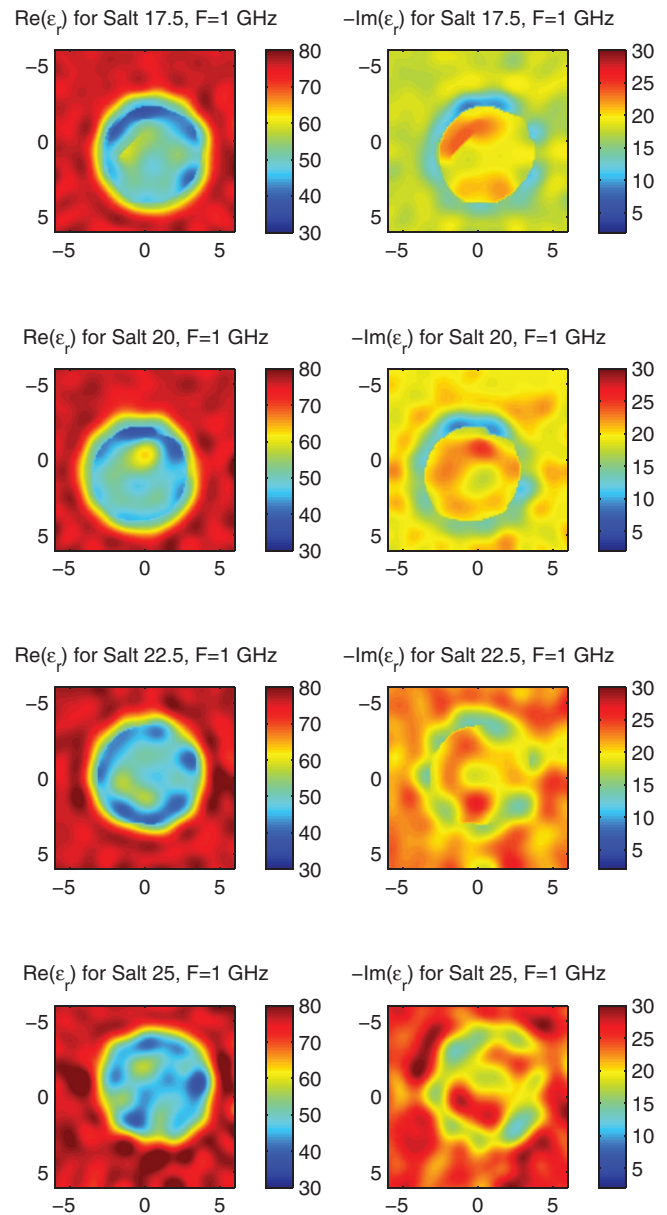


FIG. 11. Reconstruction of phantom #1 at 1.0 GHz, for four matching fluids, *Salt 17.5* through *Salt 25*. Real part of  $\epsilon$  is on the left and imaginary part on the right.

In every case, both  $L$ -norms drop with the first addition of salt to the matching fluid (i.e., going from the *Salt 4* to *Salt 10* matching fluid). In almost every case, the  $L$ -norms rise above the minimum values at the higher salt concentrations (*Salt 22.5* and *Salt 25*). The exceptions to this are the  $L$ -norms on the real reconstructions for lower frequency data sets, and we speculate that we are merely seeing the fact that the electrical distance between the antenna elements is smaller at these frequencies (and therefore the noise metric is not as strongly effected). In no case do the  $L$ -norms improve over the minimum values for the high-loss (*Salt 22.5* and *Salt 25*) data sets.

For phantom #2, the frequency of operation has a strong effect on the  $L$ -norms, particularly for the imaginary reconstructions. The effect is stronger for phantom #2 because the contrast is higher for this phantom, and higher contrasts are

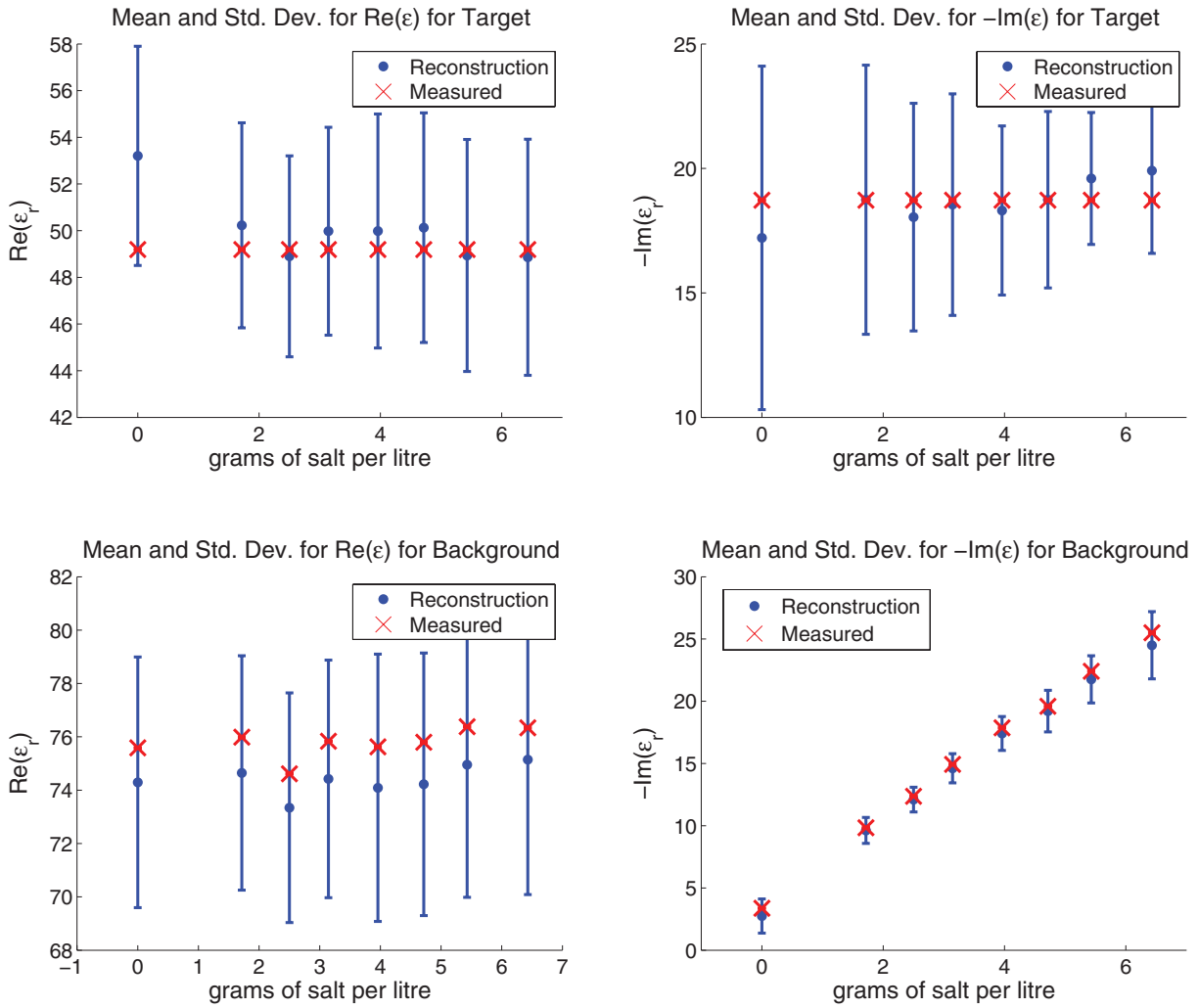


FIG. 12. Mean and standard deviation (error bars) of reconstructions for phantom #1 at 1 GHz. (Top row) Real and imaginary values of the permittivities,  $\epsilon_r$ , for the target. (Bottom row) Real and imaginary  $\epsilon_r$  of the background. Reconstruction values are shown with the dot and line, measured values shown with the x's.

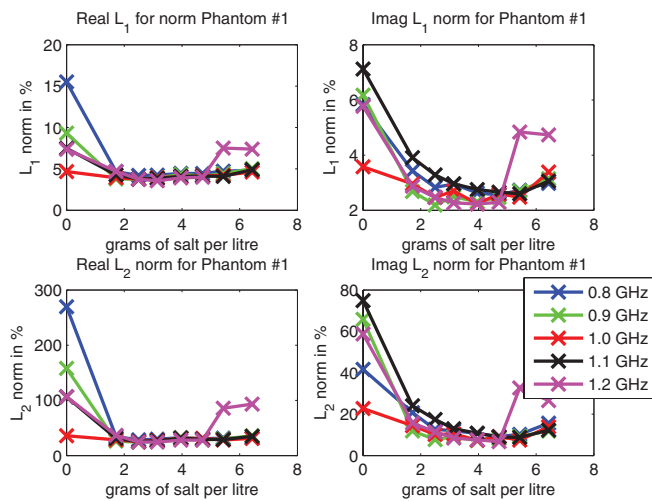


FIG. 13.  $L$ -norms for phantom #1,  $f = 0.8$ – $1.2$  GHz. Real and imaginary parts of the reconstruction are presented separately. (Top)  $L_1$ -norms for real and imaginary part of the reconstructions and (bottom)  $L_2$ -norms. Blue = 0.8 GHz, green = 0.9 GHz, red = 1 GHz, black = 1.1 GHz, and magenta = 1.2 GHz.

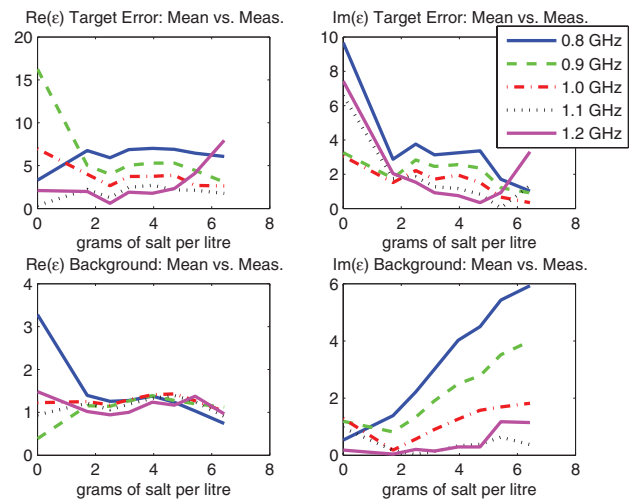


FIG. 14. Errors between measured and mean values for the target and background region of phantom #1. Real and imaginary parts of the reconstruction are presented separately. Solid = 0.8 GHz, dashed = 0.9 GHz, dash-dot = 1 GHz, dotted = 1.1 GHz, and solid = 1.2 GHz.

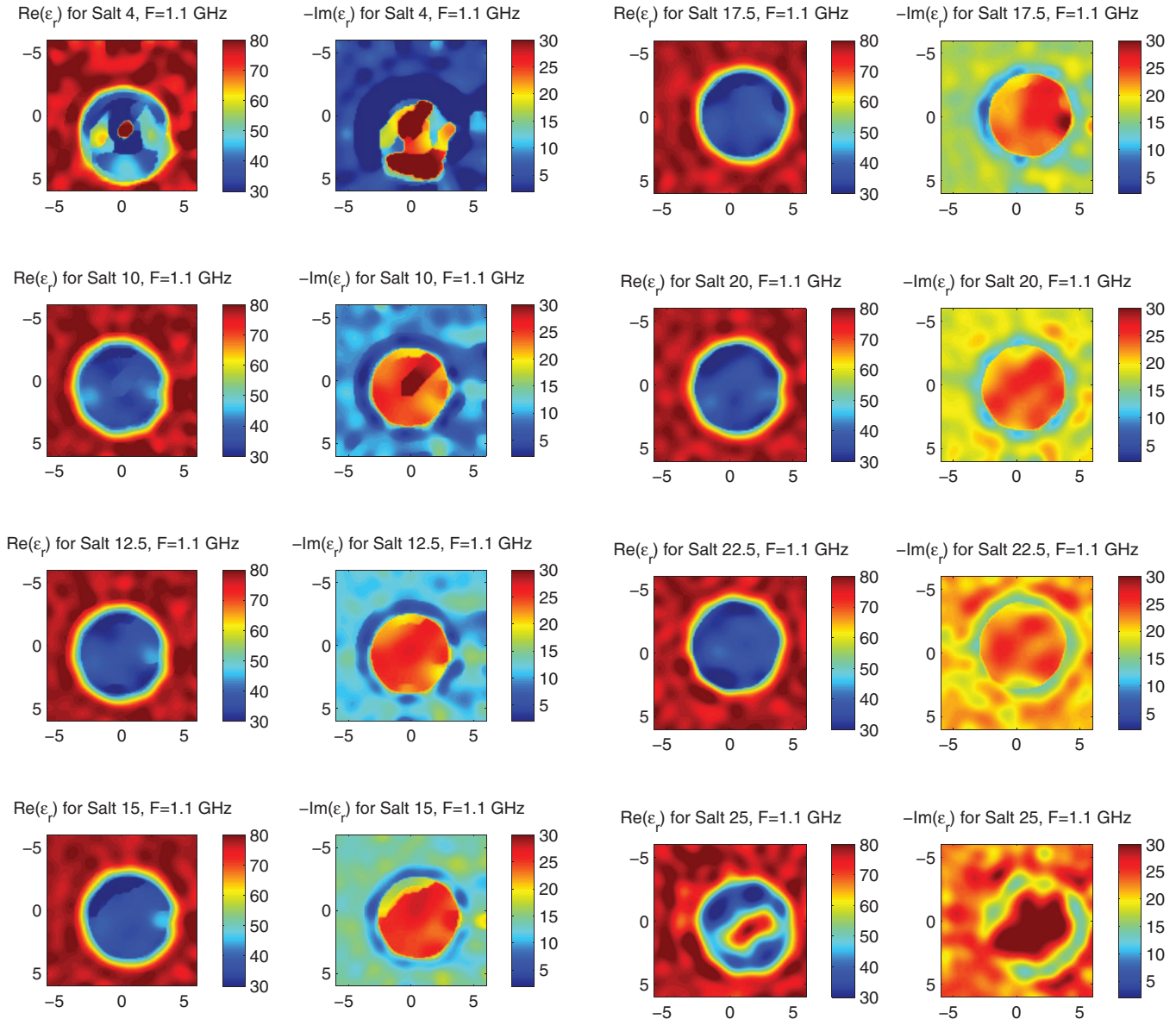


FIG. 15. Reconstruction of phantom #2 at  $f = 1.1$  GHz, for four matching fluids, *Salt 4* through *Salt 15*. Real part of  $\epsilon$  is on the left and imaginary part on the right.

FIG. 16. Reconstruction of phantom #2 at  $f = 1.1$  GHz, for four matching fluids, *Salt 17.5* through *Salt 25*. Real part of  $\epsilon$  is on the left and imaginary part on the right.

more difficult to reconstruct, particularly as the electrical size increases. The lower norms are seen for the lower frequencies (0.8, 0.9, and 1 GHz), while the higher frequencies (1.1 and 1.2 GHz) show significantly worse reconstructions, and associated higher norms.

The comparisons of the mean permittivity for each region (i.e., “target” or “background”) vs the measured permittivity, shown in Figs. 14 and 19, do not show the trade-off between modeling error and noise as clearly as the  $L$ -norms. However, the extremes of the salt densities have the worst imaging results. For example, considering the 0.8 GHz data (solid blue line) in Fig. 14, conflicting results may be seen: for the imaginary reconstruction, the target values get steadily better as the salt concentration increases, while the background reconstruction gets steadily worse. For the real metrics (left side of Fig. 14), the target reconstruction gets slightly worse as salt

concentration increases, while the background gets better as the salt increases. Taken together, these plots lead to a similar conclusion: the midlevels of salt density (approximately 2.5–4.5 g/l) provide the best trade-offs in image metrics, with a relatively broad range of acceptable losses, not a single optimum.

The noise metrics (Fig. 20) show the robustness of the imaging algorithm with respect to the value of the noise metric. Considering the worst case presented (phantom #2, 1.1 GHz, *Salt 25* data set), the noise metric is  $\approx 1.11$  (less than 1 dB), and yet the overall shape of the phantom is still readily visible in the real part of the reconstruction. However, we do note that the noise metric as defined is not a traditional signal-to-noise ratio, which takes into account white-noise (our noise metric contains additional errors in the measurement, e.g., if the target moved). Furthermore, some measured signals at

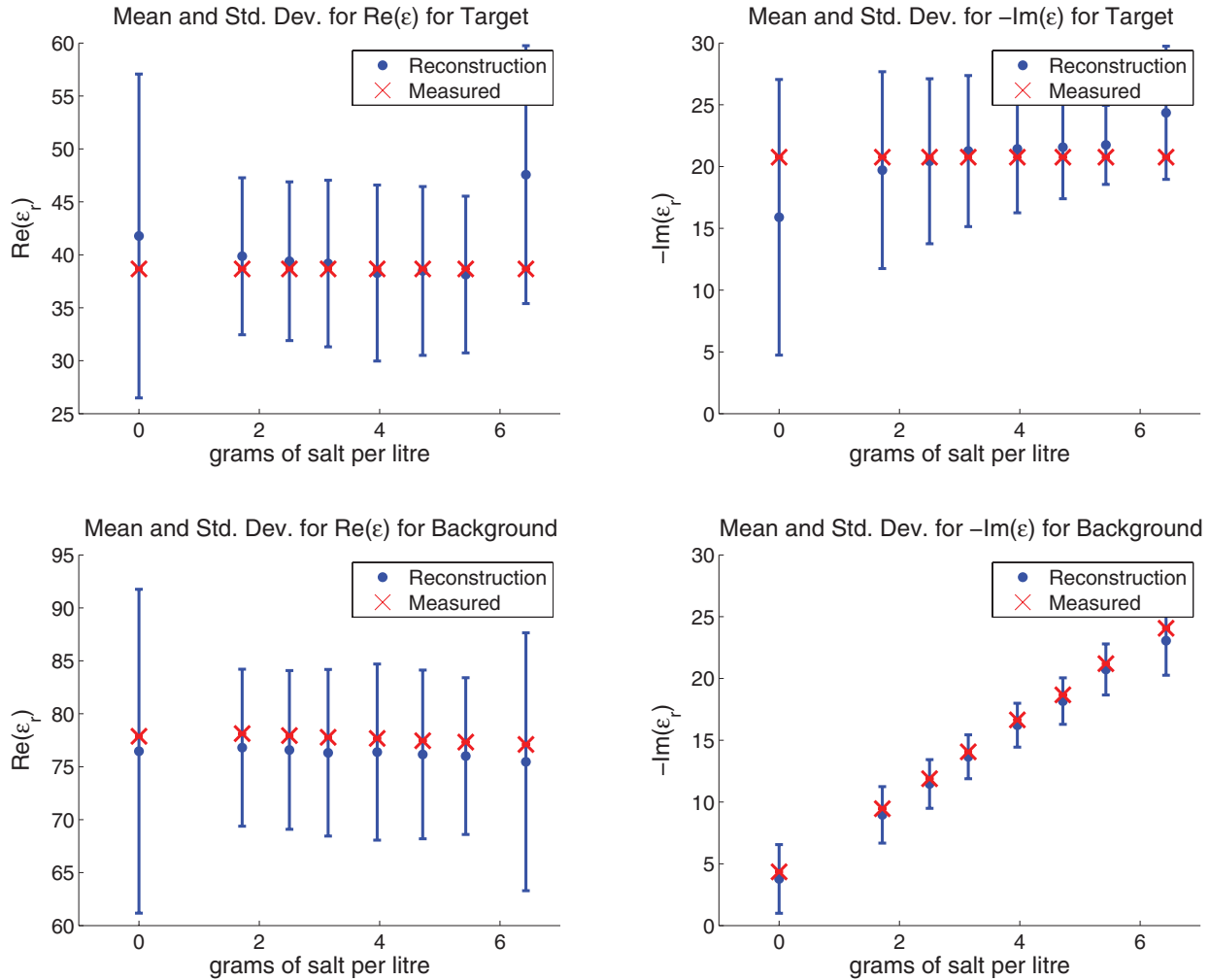


FIG. 17. Mean and standard deviation (error bars) of reconstructions for phantom #2 at 1.1 GHz. (Top row) Real and imaginary values of the permittivities,  $\epsilon$ , for the target. (Bottom row) Real and imaginary  $\epsilon$  of the background. Reconstruction values are shown with the dot and line, measured values shown with the x's.

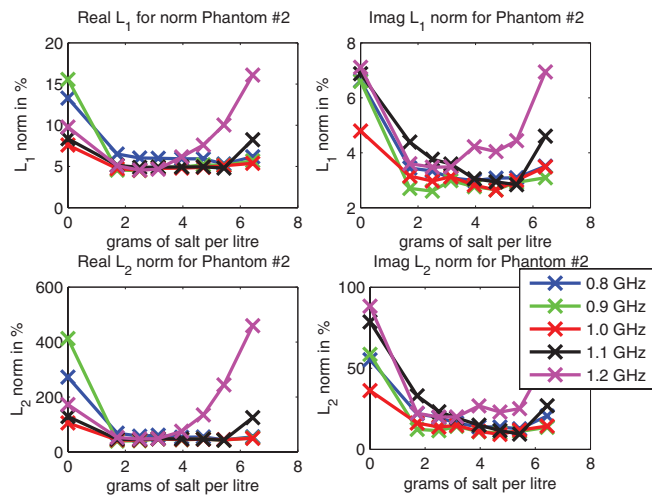


FIG. 18.  $L$ -norms for phantom #2,  $f = 0.8-1.2$  GHz. (Top)  $L_1$ -Norms for real and imaginary part of the reconstructions and (bottom)  $L_2$ -norms. Blue = 0.8 GHz, green = 0.9 GHz, red = 1 GHz, black = 1.1 GHz, and magenta = 1.2 GHz. Real and imaginary parts of the reconstruction are presented separately.

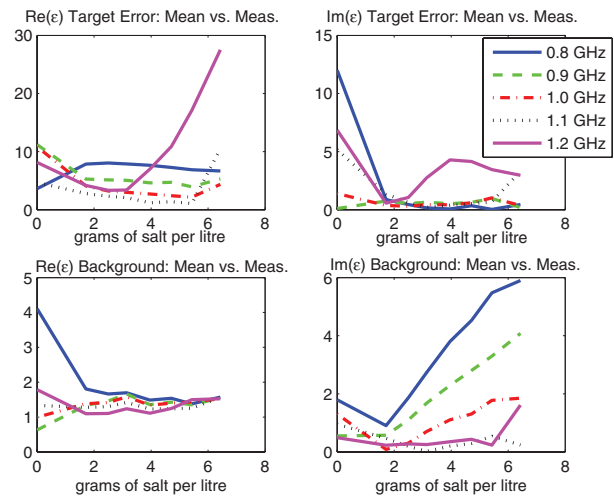


FIG. 19. Errors between measured and mean values for the target and background region of phantom #2. Solid = 0.8 GHz, dashed = 0.9 GHz, dash-dot = 1 GHz, dotted = 1.1 GHz, and solid = 1.2 GHz. Real and imaginary parts of the reconstruction are presented separately.

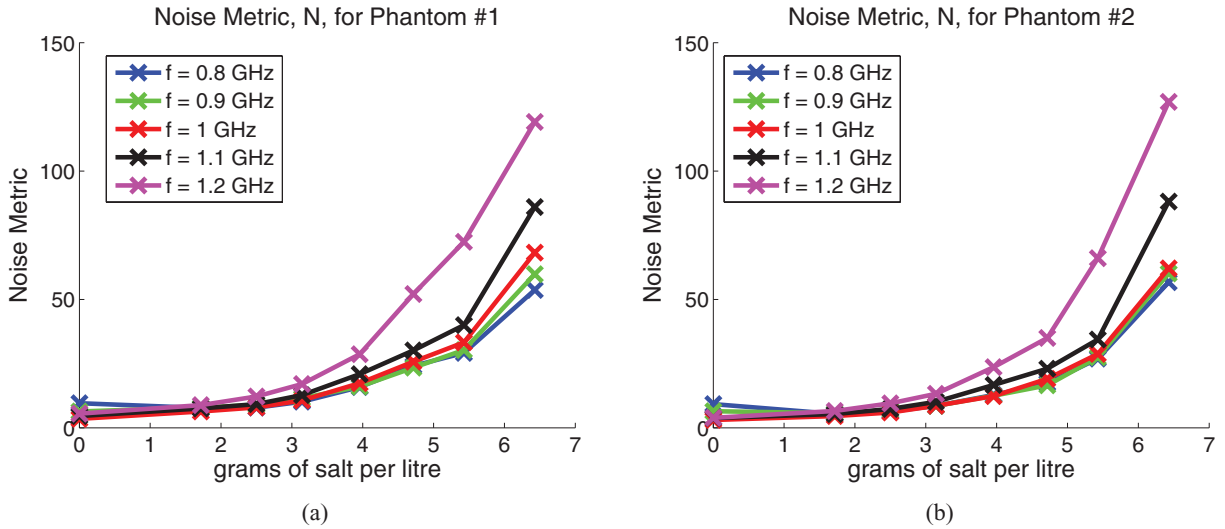


FIG. 20. Noise metric for  $f = 0.8\text{--}1.2$  GHz. (a) phantom #1 and (b) phantom #2.

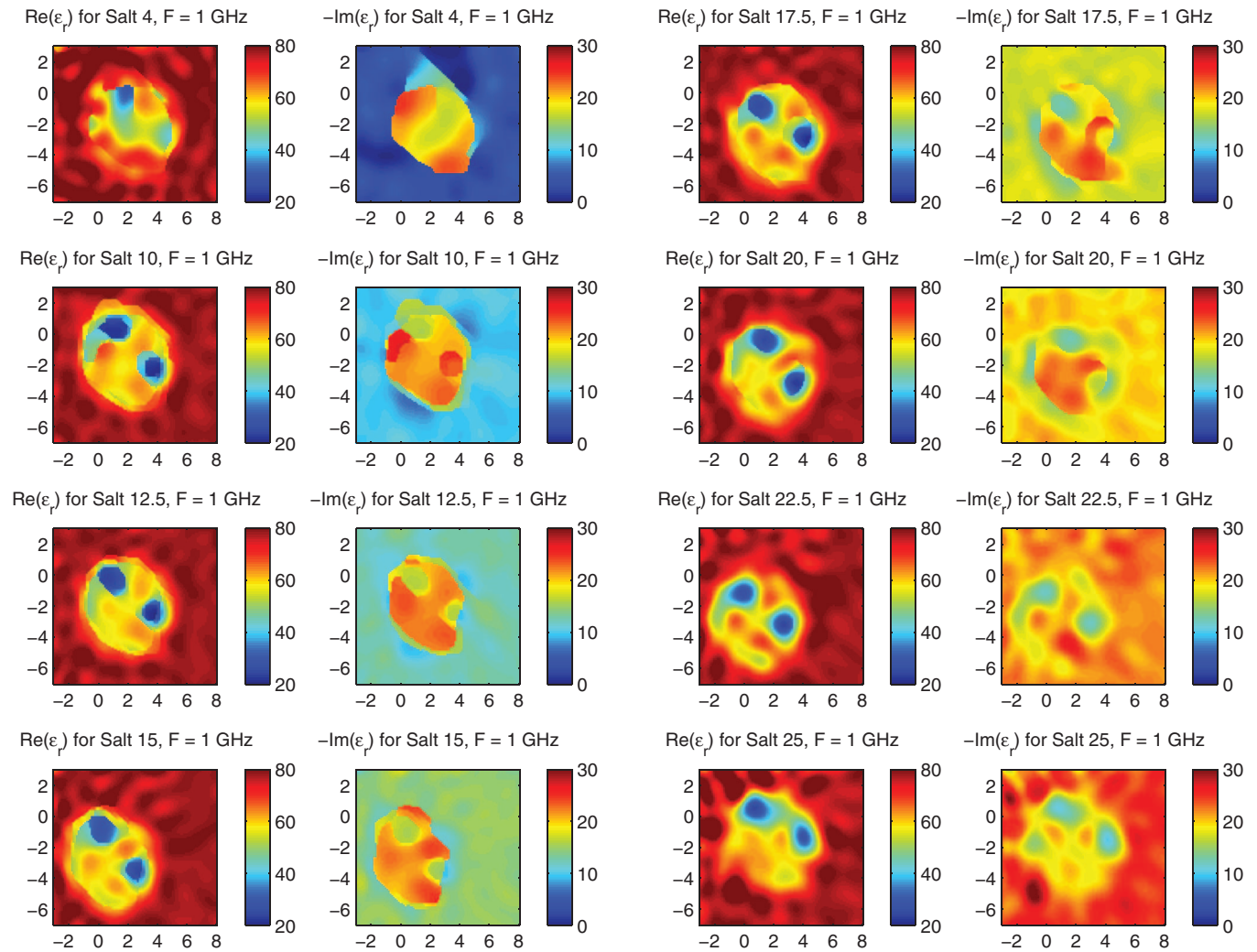


FIG. 21. Reconstruction of human forearm at  $f = 1.0$  GHz, for four matching fluids, Salt 4 through Salt 15. Real part of  $\epsilon$  is on the left and imaginary part on the right.

FIG. 22. Reconstruction of human forearm at  $f = 1.0$  GHz, for four matching fluids, Salt 17.5 through Salt 25. Real part of  $\epsilon$  is on the left and imaginary part on the right.

high salt concentrations (such as the signal  $S_{1,13}$  for the *Salt 25* data set) will consist entirely of noise and thus affect the noise metric, but will have such a small magnitude that these signals will be effectively ignored by the inversion algorithm. This could skew the noise metric to a high value, while still providing a reasonable quality image.

### VII.A. Human forearm data set

The worst images are unsurprisingly seen at the extremes, and most differences between images (particularly outside of the extreme losses) are seen in the imaginary part of the reconstruction. Qualitatively, we expect that the arm will consist of skin, a fatty tissue layer, muscle, and two bones (the radius and ulna) with similar permittivity. While no reconstruction shows the skin layer clearly, the reconstructions which show the anatomy of the arm most clearly are the *Salt 12.5* and *Salt 15* data sets (which correspond to 2.5 and 3.14 g/l). In the *Salt 12.5* and *Salt 15* reconstructions, the outline of the arm is visible, with two bones visible in both real and imaginary parts of the image, and no large artifacts where we expect to see homogeneous muscle tissue. The permittivity values for both bones are similar for the radius and ulna.

The noise metric for the human forearm data set (Fig. 23) shows a metric which is, in general, higher than that of the phantoms (e.g., a minimum of 16% instead of 10%). We expect that this is due to minor movement of the volunteer. The movement of the arm cannot be completely controlled. For our system, we ask the volunteer to rest their hand on the bottom of the tank, and we provide a support at the top of the tank to support the top of their arm. These results show the utility of the noise metric—if, for example, the volunteer had excessive movement for a particular data set, we would expect the noise figure to be very high (allowing us to detect that movement without the full imaging process).

The qualitative analysis of this human forearm data set follows the quantitative results from our simple tissue phantoms, although it is within a more restricted range of salt contents. This justifies the use of these simple phantoms and the pro-

cess used to find the optimum loss for a matching fluid for a preclinical MWT system.

## VIII. CONCLUSION

The imaging results and image metrics show the trade-off between modeling error and noise that occurs with the use of a lossy matching fluid in MWT. For low-loss matching fluid, the reconstructions are low-quality due to the modeling error, and for high-loss fluids, the reconstructions are poor due to the high noise. Most importantly, for these simple imaging phantoms, our results show that there exists a relatively broad range of salt concentrations suitable for accurate imaging, not a single best value. Salt concentrations of approximately 2.5–4.5 g/l provide the best quality image metrics for a variety of operating frequencies useful for biological imaging.

While the phantoms used in this study are homogeneous targets, and our conclusions may not be *strictly* applied for imaging inhomogeneous biological targets, these results do, at the least, provide limits for the applicable salt concentrations. We may safely conclude that the best matching fluid for biological imaging will lie somewhere in the range of 2.5–4.5 g/l, because if simple targets cannot be reconstructed well, then more complicated targets will be even worse. For the human forearm results presented in this paper we can state that we have qualitatively determined the best results for this volunteer are at 2.5 and 3.14 g/l of salt. The restricted range provided by the simple phantom analysis allows us to restrict the number of fluids used for volunteer imaging, increasing the volunteer throughput for future studies.

We also note that these results are only strictly applicable to our exact MWT system and inversion algorithm, however we do expect these results to apply to most other MWT systems of similar electrical dimensions. If other MWT systems are significantly different to the system outlined herein (in matching fluid, frequency, antenna type, or physical configuration), the process outlined in this paper remains applicable to selecting the loss in the matching fluid.

## ACKNOWLEDGMENTS

The authors recognize the financial support of Western Economic Diversification Canada, Natural Sciences and Engineering Research Council of Canada, and CancerCare Manitoba. The authors also thank the University of Manitoba Nano-Systems Fabrication Lab for supplying the deionized water.

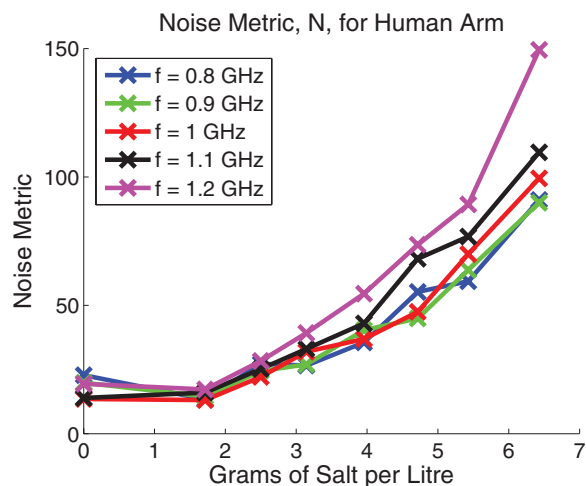


FIG. 23. Noise metric for  $f = 0.8$ – $1.2$  GHz for the human forearm data set.

<sup>a)</sup> Author to whom correspondence should be addressed. Electronic mail: colin.g.gilmore@gmail.com.

<sup>1</sup> S. Semenov, J. Kellam, U. Sizov, A. Nazarov, T. Williams, B. Nair, A. Pavlovsky, V. Posukh, and M. Quinn, "Microwave tomography of extremities. 1. Dedicated 2D system and physiological signatures," *Phys. Med. Biol.* **56**, 2005–2017 (2011).

<sup>2</sup> S. Semenov, J. Kellam, B. Nair, T. Willimas, M. Quinn, Y. Sizov, A. Nazarov, and A. Pavlovsky, "Microwave tomography of extremities. 2. Functional fused imaging of flow reduction and simulated compartment syndrome," *Phys. Med. Biol.* **56**, 2019–2030 (2011).

- <sup>3</sup>P. M. Meaney, M. W. Fanning, T. Reynolds, C. J. Fox, Q. Fang, C. A. Kogel, S. P. Poplack, and K. D. Paulsen, "Initial clinical experience with microwave breast imaging in women with normal mammography," *Acad. Radiol.* **14**, 207–218 (2007).
- <sup>4</sup>S. Poplack, S. P. Poplack, T. D. Tosteson, W. A. Wells, B. W. Pogue, P. M. Meaney, A. Hartov, C. A. Kogel, S. K. Soho, J. J. Gibson, and K. D. Paulsen, "Electromagnetic breast imaging results of a pilot study in women with abnormal mammograms," *Radiology* **243**, 350–359 (2007).
- <sup>5</sup>E. Fear, P. Meaney, and M. Stuchly, "Microwaves for breast cancer detection?" *IEEE Potentials* **22**(1), 12–18 (2003).
- <sup>6</sup>J. M. Sill and E. Fear, "Tissue sensing adaptive radar for breast cancer detection: Study of immersion liquids," *Electron. Lett.* **41**(3), 113–115 (2005).
- <sup>7</sup>L. van Nieuwstadt, "Microwave measurement system for breast cancer imaging: An experimental prototype towards time-domain inverse scattering," Ph.D. dissertation (University of Michigan, 2011).
- <sup>8</sup>E. Fear, S. Hagness, P. Meaney, M. Okoniewski, and M. Stuchly, "Enhancing breast tumor detection with near-field imaging," *IEEE Microw. Mag.* **3**(1), 48–56 (2002).
- <sup>9</sup>R. K. Amineh, M. Ravan, A. Trehan, and N. K. Nikolova, "Near-field microwave imaging based on aperture raster scanning with TEM horn antennas," *IEEE Trans. Antennas Propag.* **59**(3), 928–940 (2011).
- <sup>10</sup>D. Winters, E. Bond, B. Van Veen, and S. Hagness, "Estimation of the frequency-dependent average dielectric properties of breast tissue using a time-domain inverse scattering technique," *IEEE Trans. Antennas Propag.* **54**(11), 3517–3528 (2006).
- <sup>11</sup>Z. Q. Zhang and Q. H. Liu, "Three-dimensional nonlinear image reconstruction for microwave biomedical imaging," *IEEE Trans. Biomed. Eng.* **51**(3), 544–548 (2004).
- <sup>12</sup>P. Kosmas and C. M. Rappaport, "FDTD-based time reversal for microwave breast cancer detection—localization in three dimensions," *IEEE Trans. Microw. Theory Techn.* **54**(4), 1921–1927 (2006).
- <sup>13</sup>M. El-Shenawee and E. Miller, "Spherical harmonics microwave algorithm for shape and location reconstruction of breast cancer tumor," *IEEE Trans. Med. Imaging* **25**(10), 1258–1271 (2006).
- <sup>14</sup>M. Klemm, I. Craddock, J. Leendertz, A. Preece, D. Gibbins, M. Shere, and R. Benjamin, "Clinical trials of a uwb imaging radar for breast cancer," in *2010 Proceedings of the Fourth European Conference on Antennas and Propagation (EuCAP)* (IEEE, Barcelona, Spain, 2010), pp. 1–4.
- <sup>15</sup>M. Klemm, I. J. Craddock, J. A. Leendertz, A. Preece, and R. Benjamin, "Radar-based breast cancer detection using a hemispherical antenna array—Experimental results," *IEEE Trans. Antennas Propag.* **57**(6), 1692–1704 (2009).
- <sup>16</sup>P. Meaney, S. Pendergrass, M. Fanning, D. Li, and K. Paulsen, "Importance of using a reduced contrast coupling medium in 2D microwave breast imaging," *J. Electromagn. Waves Appl.* **17**, 333–355 (2003).
- <sup>17</sup>S. Semenov, A. Bulyshev, A. Abubakar, V. Posukh, Y. Sizov, A. Souvorov, P. van den Berg, and T. Williams, "Microwave-tomographic imaging of the high dielectric-contrast objects using different image-reconstruction approaches," *IEEE Trans. Microw. Theory Techn.* **53**(7), 2284–2294 (2005).
- <sup>18</sup>S. Semenov, "Microwave tomography: Review of the progress towards clinical applications," *Philos. Trans. R. Soc. London, Ser. A* **367**(1900), 3021–3042 (2009).
- <sup>19</sup>K. Paulsen, P. Meaney, and L. Gilman, *Alternative Breast Imaging: Four Model-Based Approaches* (Springer-Verlag, New York, 2005).
- <sup>20</sup>P. Meaney, K. Paulsen, S. Geimer, S. Haider, and M. Fanning, "Quantification of 3-D field effects during 2-D microwave imaging," *IEEE Trans. Biomed. Eng.* **49**(7), 708–720 (2002).
- <sup>21</sup>C. Gilmore and J. LoVetri, "Enhancement of microwave tomography through the use of electrically conducting enclosures," *Inverse Probl.* **24**, 035008 (2008).
- <sup>22</sup>L. Crocco and A. Litman, "On embedded microwave imaging systems: Retrievable information and design guidelines," *Inverse Probl.* **25**, 065001 (2009).
- <sup>23</sup>P. Mojabi and J. LoVetri, "Eigenfunction contrast source inversion for circular metallic enclosures," *Inverse Probl.* **26**, 025010 (2010).
- <sup>24</sup>A. Zakaria, C. Gilmore, and J. LoVetri, "Finite-element contrast source inversion method for microwave imaging," *Inverse Probl.* **26**, 115010 (2010).
- <sup>25</sup>K. Paulsen and P. Meaney, "Nonactive antenna compensation for fixed-array microwave imaging. I. model development," *IEEE Trans. Med. Imaging* **18**(6), 496–507 (1999).
- <sup>26</sup>M. Haynes and M. Moghaddam, "Multipole and s-parameter antenna and propagation model," *IEEE Trans. Antennas Propag.* **99**, 1–1 (2011).
- <sup>27</sup>M. Haynes, S. Clarkson, and M. Moghaddam, "Electromagnetic inverse scattering algorithm and experiment using absolute source characterization," in *2011 IEEE International Symposium on Antennas and Propagation (APSURSI)* (IEEE, Spokane, Washington, 2011), pp. 2545–2548.
- <sup>28</sup>P. Kosmas, J. Shea, B. V. Veen, and S. Hagness, "Three-dimensional microwave imaging of realistic breast phantoms via an inexact gauss-newton algorithm," in *IEEE Antennas and Propagation Symposium*, San Diego, USA, 2008.
- <sup>29</sup>D. Winters, J. Shea, P. Kosmas, B. Van Veen, and S. Hagness, "Three-dimensional microwave breast imaging: Dispersive dielectric properties estimation using patient-specific basis functions," *IEEE Trans. Med. Imaging* **28**(7), 969–981 (2009).
- <sup>30</sup>A. E. Bulyshev, A. Souvorov, S. Semenov, R. H. Svenson, A. Nazarov, Y. Sizov, and G. P. Tatsis, "Three-dimensional microwave tomography. Theory and computer experiments in scalar approximation," *Inverse Probl.* **16**, 863–875 (2000).
- <sup>31</sup>Q. Fang, P. Meaney, and K. Paulsen, "Viable three-dimensional medical microwave tomography: Theory and numerical experiments," *IEEE Trans. Antennas Propag.* **58**(2), 449–458 (2010).
- <sup>32</sup>C. Rappaport, "Determination of bolus dielectric constant for optimum coupling of microwaves through skin for breast cancer imaging," *Int. J. Antennas Propag.* **2008**, 359582 (2008).
- <sup>33</sup>A. Zakaria, C. Gilmore, S. Pistorius, and J. LoVetri, "Balanced multiplicative regularization for the contrast source inversion method," in *The 28th International Review of Progress in Applied Computational Electromagnetics Conference*, Columbus, OH, 2012.
- <sup>34</sup>P. M. van den Berg and A. Abubakar, "Contrast source inversion method: State of art," *Prog. Electromagn. Res.* **34**, 189–218 (2001).
- <sup>35</sup>P. M. van den Berg and R. E. Kleinman, "A contrast source inversion method," *Inverse Probl.* **13**, 1607–1620 (1997).
- <sup>36</sup>P. Mojabi and J. LoVetri, "A pre-scaled multiplicative regularized gauss-newton inversion," *IEEE Trans. Antennas Propag.* **59**, 2954–2963 (2011).
- <sup>37</sup>P. Meaney, N. Yagnamurthy, and K. Paulsen, "Pre-scaled two-parameter gauss-newton image reconstruction to reduce property recovery imbalance," *Phys. Med. Biol.* **47**, 1101 (2002).
- <sup>38</sup>C. Gilmore, P. Mojabi, A. Zakaria, M. Ostadrahimi, C. Kaye, S. Noghianian, L. Shafai, S. Pistorius, and J. LoVetri, "A wideband microwave tomography system with a novel frequency selection procedure," *IEEE Trans. Biomed. Eng.* **57**(4), 894–904 (2010).